Supplement of Nat. Hazards Earth Syst. Sci., 22, 3167–3182, 2022
https://doi.org/10.5194/nhess-22-3167-2022-supplement
© Author(s) 2022. CC BY 4.0 License.

Natural Hazards and Earth System Sciences
Open Access
EGU

Supplement of

Partitioning the contributions of dependent offshore forcing conditions in the probabilistic assessment of future coastal flooding

Jeremy Rohmer et al.

Correspondence to: Jeremy Rohmer (j.rohmer@brgm.fr)

The copyright of individual parts of the supplement might differ from the article licence.

- **Supplementary Materials S1 Dependence Analysis**
- **Supplementary Material S2 Extreme value analysis - Marginals**
- **Supplementary Materials S3 GSA with first-order Sobol' indices**
- **Supplementary Materials S4 Differences between DEM 2015 and 2008**
- **Supplementary Materials S5 Influence of the modelling choices**

Supplementary Materials S1 Dependence Analysis

First, we provide the matrix of pairwise correlation coefficients (considering two types of correlation, i.e. Pearson and Kendall) calculated for the database of hindcasts (Sect. 2.2) used to perform the multivariate extreme value analysis.

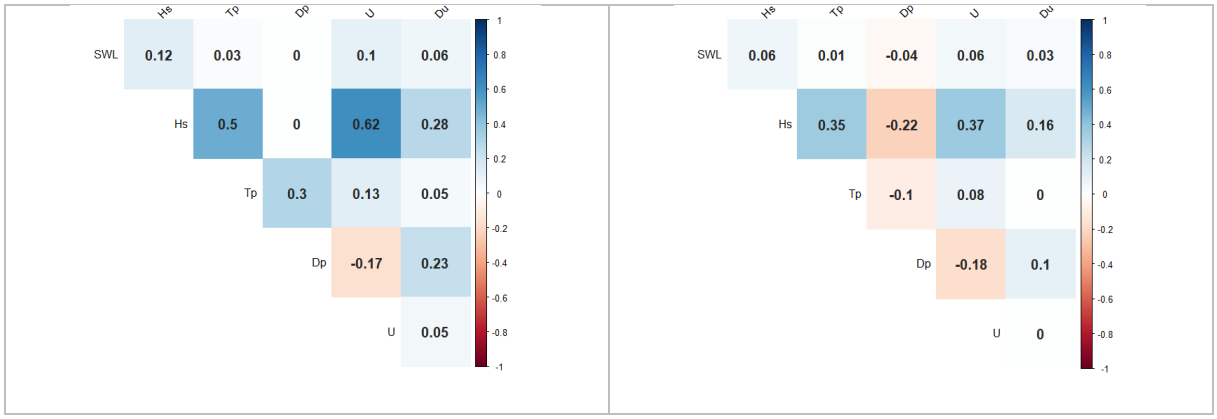

Figure S1. Pairwise correlation coefficients for the offshore forcing conditions (Pearson – left, Kendall - right)

Second, we provide insights in the extremal dependence, i.e. the dependence when the considered variables take large value. To do so, we focus on the empirical estimates of $\bar{\chi}$ of summary statistics as defined by Coles et al. (1999) defined as follows:

$$\bar{\chi} = \lim_{u \to 1} \left(\frac{2\log(P(U > u))}{\log(P(U > u \cap V > u))} - 1 \right)$$

where *U*, *V* are the two different forcing conditions, *u* is the quantile level. This indicator is used to screen locations where extremal dependence between both variables is exhibited: this is indicated where the $\bar{\chi}$ tends to 1.0 for very large quantile level *u* of both variables. The evaluation of $\bar{\chi}$ on the hindcast database shows that this remains below 1.0 in the limiting case hence indicating asymptotic independence. In this class of extremal dependence, $\bar{\chi}$ further provides a measure of the strength of dependence. Table S1 shows that this strength reaches non negligible values (>0). The same analysis was conducted on the randomly generated samples (Table S2) and shows that the extremal dependence is relatively well reproduced. We note that the differences are larger for (*Hs*, *SWL*) but these can be considered satisfactory given the relatively large width of the confidence intervals (values in brackets).

Table S1. $\bar{\chi}$ value for the hindcast database. Values in brackets correspond to the bounds of the 95% confidence interval

	SWL	*Hs*
Hs	0.33 (0.10, 0.57)	
U	0.28 (0.06, 0.50)	0.46 (0.20, 0.70)

Table S2. $\bar{\chi}$ value for the randomly generated samples. Values in brackets correspond to the bounds of the 95% confidence interval

	SWL	*Hs*
Hs	0.74 (0.42, 1.00)	
U	0.31 (0.08, 0.56)	0.48 (0.22, 0.76)

Finally, we analyze in more details in Table S3 the values of the (a,b)-parameters (as defined in Eq. 4) of the dependence model. Note that the values should be read columnwise, which means that the value of the first column correspond to the (a,b)- parameters when *SWL* is used as the conditional variable in Eq. 4. As discussed by Heffernan and Tawn (2004), their semi-parametric model allows to cover different types of extremal dependence with the following general rules:

For $2 \leq j \leq d$,

- When $a_j=1$ and $b_j=0$, the variables (X_1, X_j) are asymptotically dependent;

- When $a_j<1$, the variables (X_1, X_j) are asymptotically independent.

In this latter case,

- When $0<a_j<1$ or $a_j=0$ and $b_j>0$, means positive dependence;
- When $a_j=b_j=0$, means near independence.

Table S3 clearly shows a non-negligible positive strength of dependence in the class of asymptotic independence (as indicated by $0<a_j<1$).

Table S3. (a,b)-parameters of the dependence model.

	SWL	Hs	U
SWL		(0.189, 0.186)	(0.514, 0.365)
Hs	(0.357, -0.10)		(0.193, 0.145)
U	(0.275, 0.10)	(0.629, 0.242)	

Supplementary Material S2 Diagnostics of the marginals

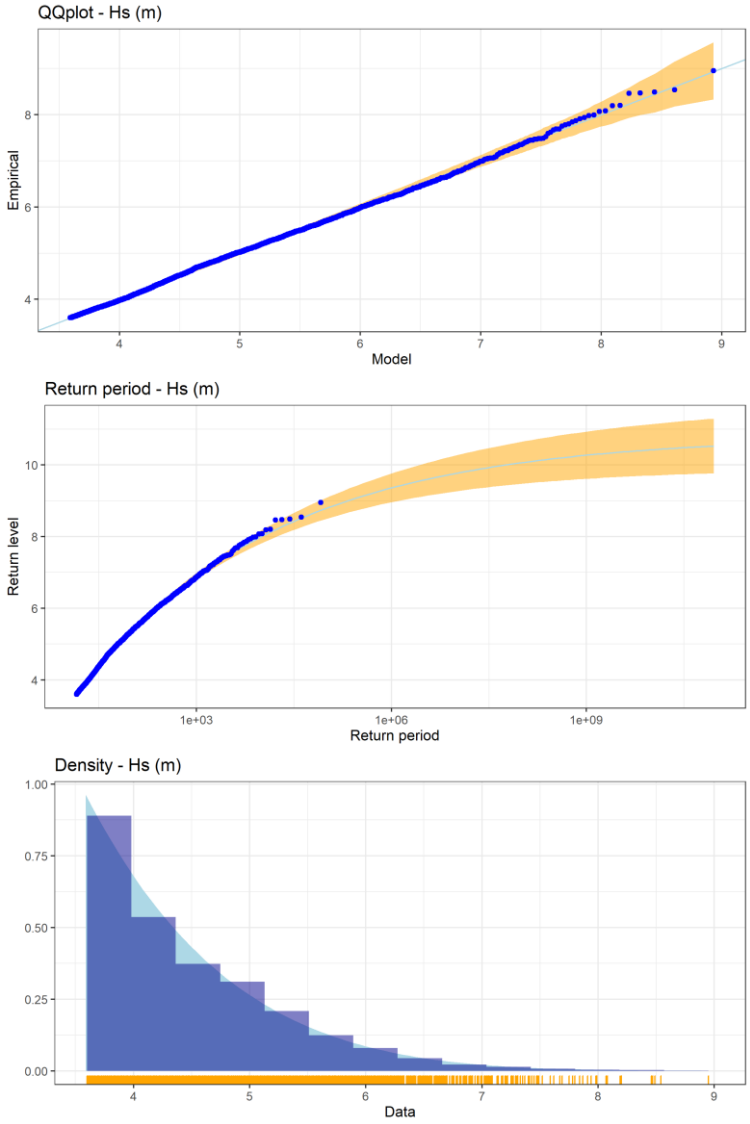

Figure S2: Diagnostic plots for the GPD fitted to *Hs*. (a) Quantile-Quantile plot (the band is the 95% confidence envelope); (b) Return level plot (the return period is expressed in number of events); (c) Comparison between the empirical and the theoretical density distribution.

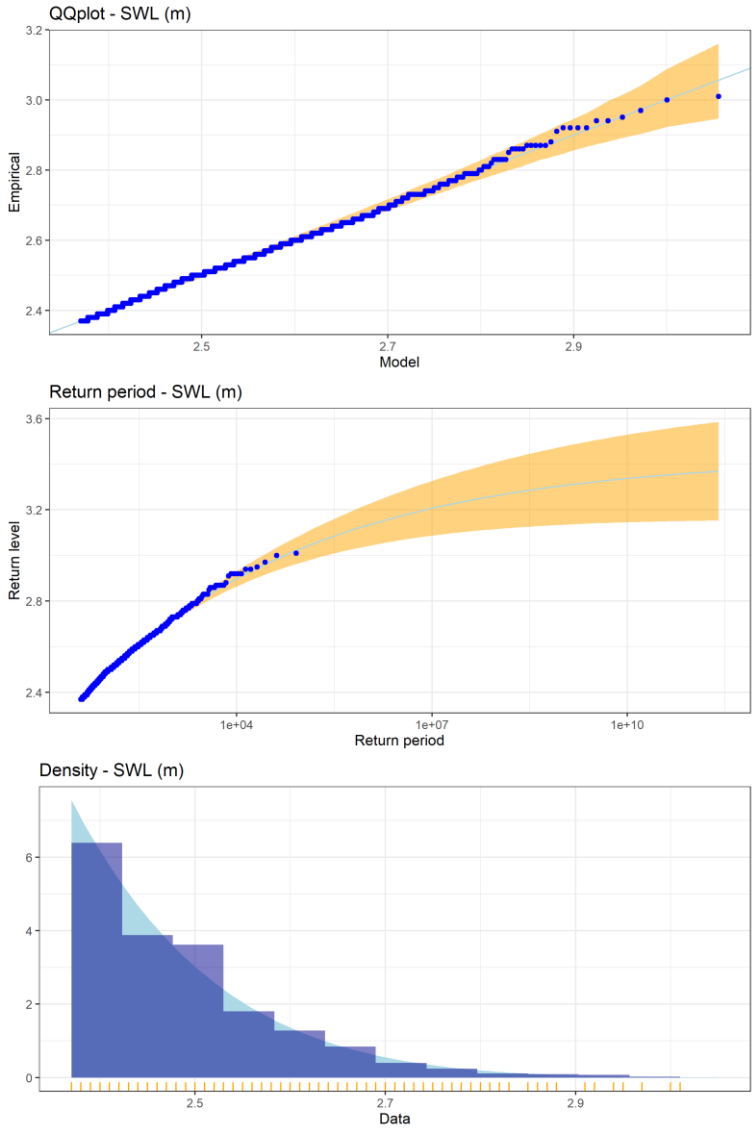

Figure S3: Diagnostic plots for the GPD fitted to *SWL*. (a) Quantile-Quantile plot (the band is the 95% confidence envelope); (b) Return level plot (the return period is expressed in number of events); (c) Comparison between the empirical and the theoretical density distribution.

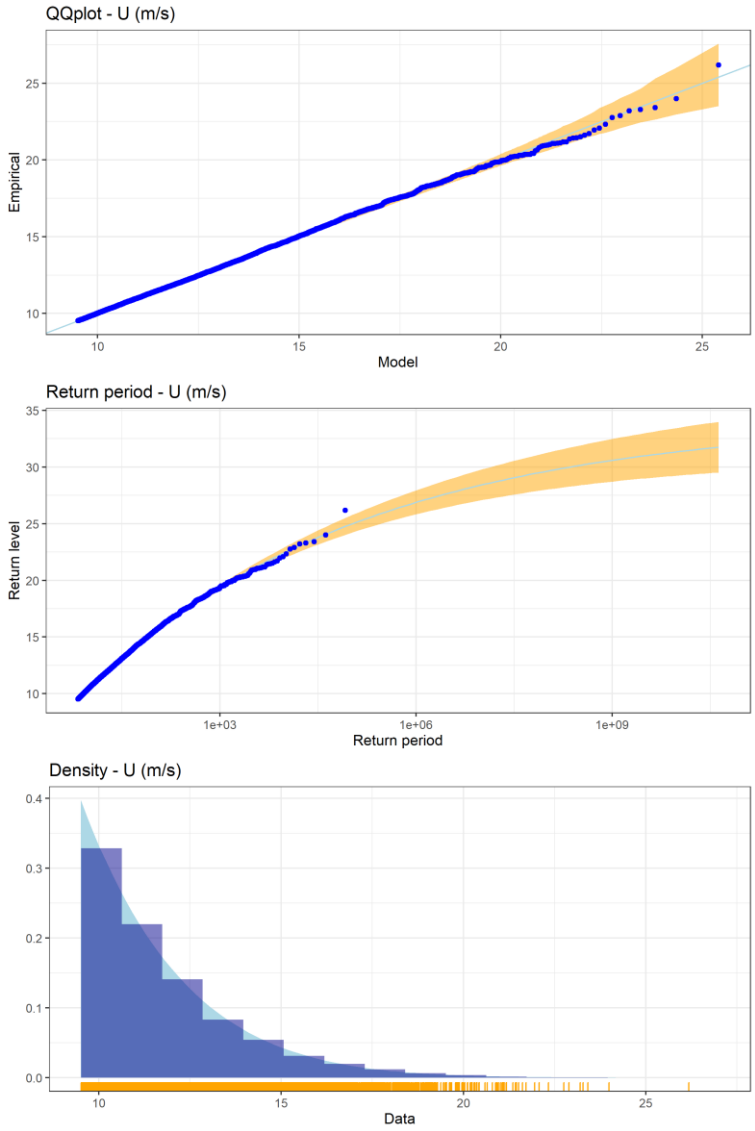

Figure S4: Diagnostic plots for the GPD fitted to *U*. (a) Quantile-Quantile plot (the band is the 95% confidence envelope); (b) Return level plot (the return period is expressed in number of events); (c) Comparison between the empirical and the theoretical density distribution.

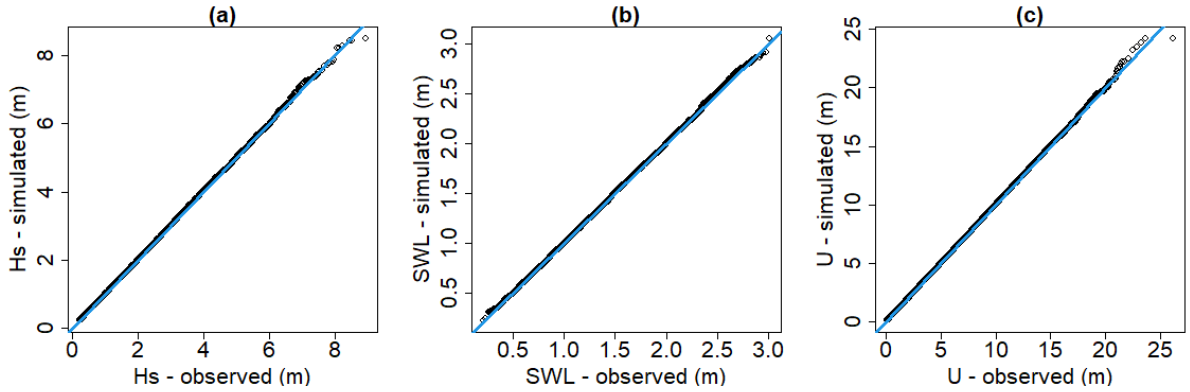

Figure S5: Quantile-Quantile plot considering the observations (hindcast) and the N=50,000 randomly simulated samples for *Hs* (a), *SWL* (b), and *U* (c).

Supplementary Materials S3 GSA with first-order Sobol' indices

Figure S6 provides the GSA results using the first-order Sobol' indices (which do not account for the dependence among the variables, see Sect. 3.4). This shows that the identification of the major contributors to the uncertainty would have been similar, i.e. high influence of *SWL* in the short term, and an increase impact of *SLR* until reaching an overwhelming role in the very long term. Yet, the interpretation of the importance of the remaining variables would have been more difficult, if not leading to wrong conclusions. Before 2100, we note very low values of the corresponding 1st order Sobol' indices from which a low influence could have been concluded. Yet, these indices account neither for the interaction terms (measured by one minus the sum of all 1st order indices as outlined by the large white area in Fig. S6) nor for the dependence (as clearly shown in Fig. 3). Here, the Shapley effects are useful to clearly indicate the significant (though moderate) importance of these variables, and more importantly they provide a strong evidence that the wave and wind characteristics have all minor influence in the very long term because of their low Shapley effect values.

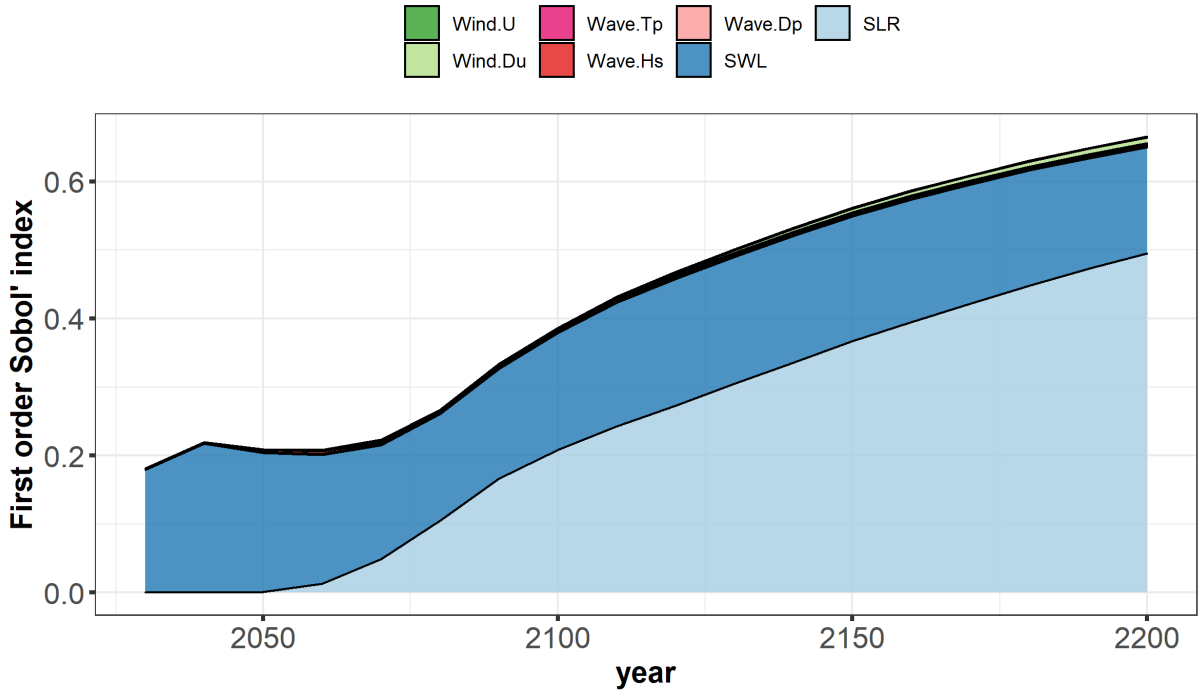

Figure S6: Time evolution of the first-order Sobol' indices for the base case (RCP4.5, Y_C=2,000m3, DEM 2015 and use of the median value to account for wave stochasticity) estimated by computing the median value from 50 replicates of the estimation procedure (Sect. 3.5) accounting for GP and sampling error.

Supplementary Materials S4 Differences between DEM 2015 and 2008

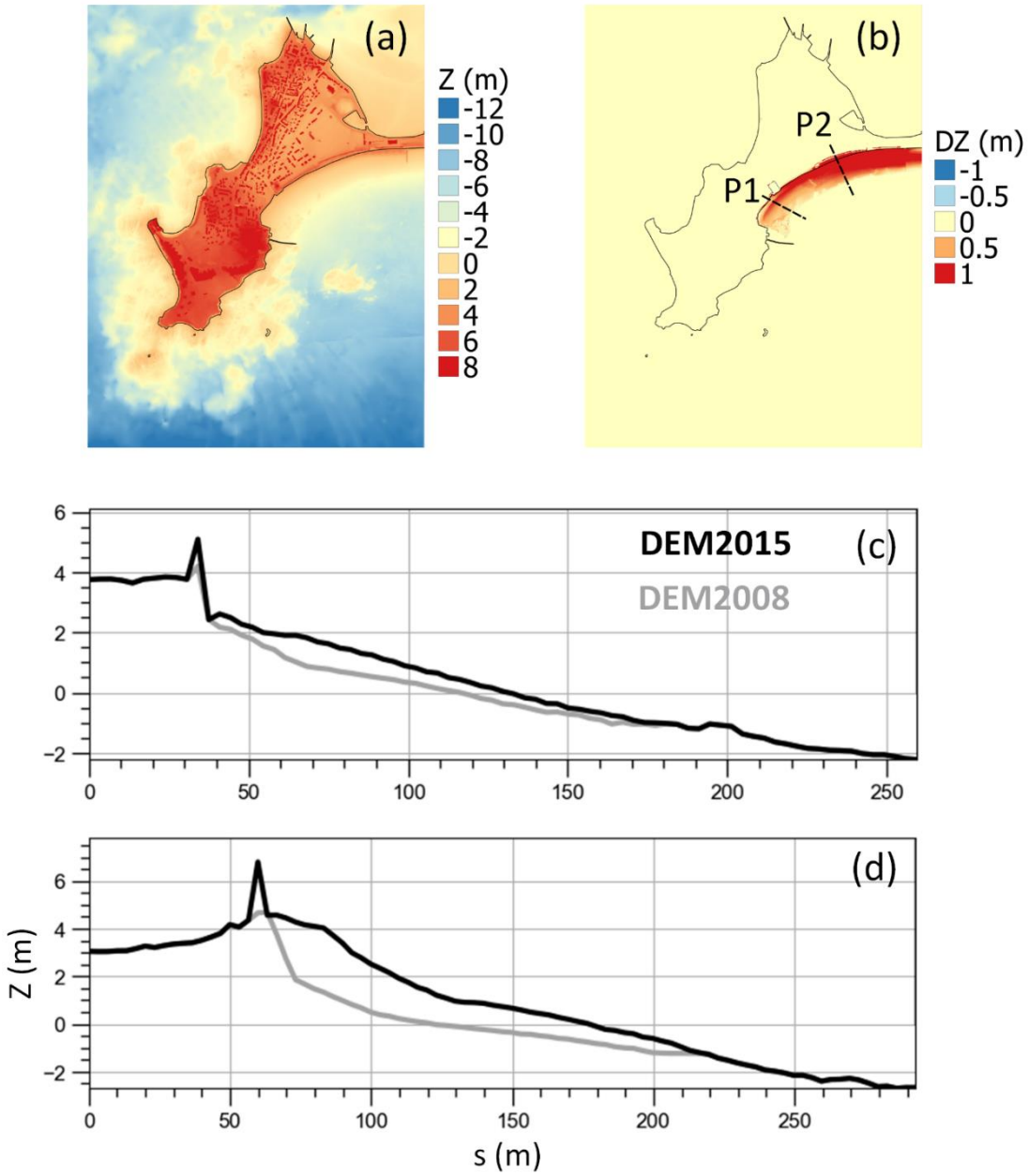

Figure S7: DEM 2015 (a); Difference (denoted DZ) between DEM 2015 and DEM 2008 (b); Elevation for DEM 2015 and 2008 along transects P1 (c) and P2 (d).

Supplementary Materials S5 Influence of the modelling choices

Here, we investigate to which extent alternative scenario assumptions underlying our approach might change the afore-described conclusions, namely: the volume threshold Y_C used to define when a flooding event occurs; the RCP scenario; the use of an alternative DEM; and the impact of wave stochasticity. For each analysis, the corresponding assumption was changed and the whole analysis was re-conducted, i.e. (1) new hydrodynamic simulations; (2) training of new GP models (the predictive capability is provided in Table S4); (3) GP-based estimate of the flooding probability and of the Shapley effects within a Monte-Carlo-based simulation procedure.

Table S4. Statistics of the performance indicator Q^2 (calculated across the folds) of the different GP metamodels calculated using a 10-fold cross validation procedure.

GP model	Median of Q^2 (%)	Interquartile of Q^2 (%)	Analysis
Median Q_{50}, DEM 2015	99.35	1.25	Sect. 4
3rd quartile Q_{75}, DEM 2015	99.22	1.12	Sect. E4
1st quartile Q_{25}, DEM 2015	99.45	1.73	Sect. E4
Median Q_{50}, DEM 2008	95.97	3.81	Sect. E3

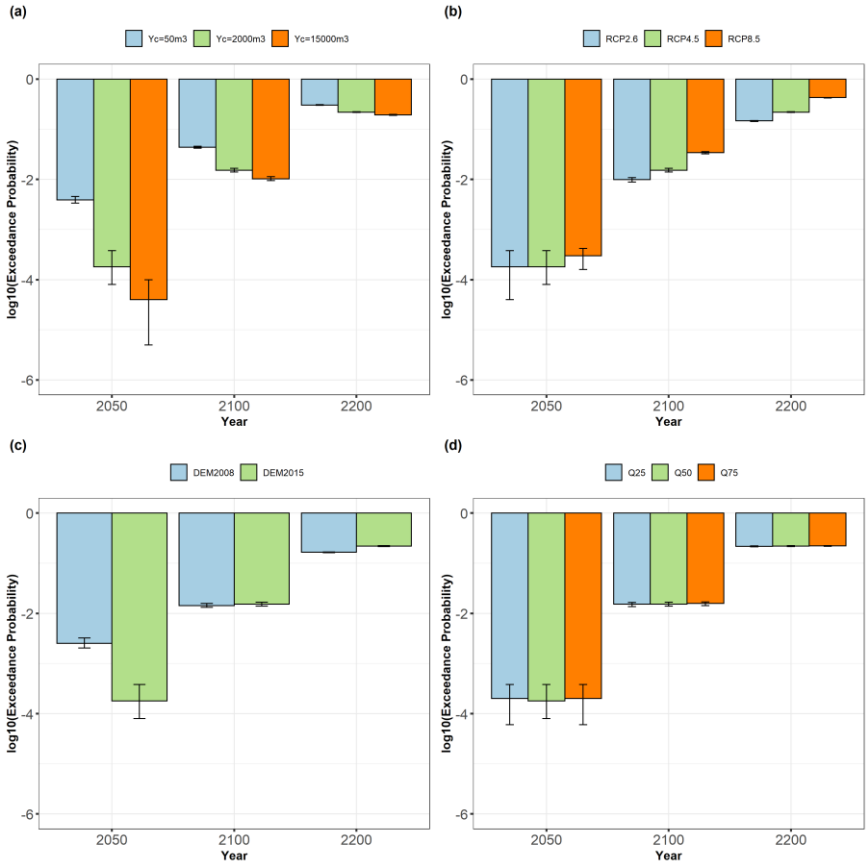

Figure S8: Flooding probability (log_{10}-transformed) at different time instants for different assumptions: volume threshold Y_C (a); RCP scenarios (b); DEM (c); and wave stochasticity modelled with different quartiles (respectively denoted Q_{25}, Q_{50} and Q_{75}) (d). The inserted figures indicate the small uncertainty band's width estimated with the lower and upper bound computed for B=50 replicates of the estimation approach (Sect. 3.5) accounting for GP and sampling error. The lines correspond to the median value computed for 50 replicates. The green lines represent the base case (defined for the median value Q_{50} of Y with a threshold of Y_C=2,000m^3 given RCP4.5 and the DEM 2015). Note that the different flooding probability estimates for (d) overlap due to minor influence of wave stochasticity.

1. Influence of the volume threshold

The uncertainty partitioning in Sect. 4 was performed given a threshold Y_C=2,000m3 that determines whether a flooding event occurs or not. The analysis is here re-conducted by respectively focusing on minor and very large flooding events defined for Y_C=50 and 15,000m^3 (as illustrated in Fig. 2).

Fig. S8(a) shows the time evolution of the flooding probability for the three cases. Compared to the base case (outlined in green), the results indicate that the occurrence of the minor (respectively very large) flooding events have a higher (lower) probability by ~8% (~-3%) in the very long term (2200). The time evolution of the uncertainty contribution is modified depending on the chosen threshold (Fig. S9). When Y_C=50m^3, *SWL* has the higher contribution (of 37%) in the short term (compare the blue with the green and orange bars in Fig. S9a), while the other offshore conditions all have lower influence (with Shapley effects of ~9-13%). Over time (Fig. S9b,c), the case Y_C=50m^3 presents a slower increase of *SLR* influence, which is directly translated into a slower reduction of *SWL* contribution (compare the two first groups of bars in Fig. S9c).

This *SLR*-threshold relation directly reflects how *SLR* acts on the flooding likelihood: it acts as an "offset", which means that it induces a higher sea water level at the coast; hence a higher likelihood of flooding. Thus, the lower the threshold value, the lower the necessary *SLR* magnitude to induce flooding, hence the lower influence.

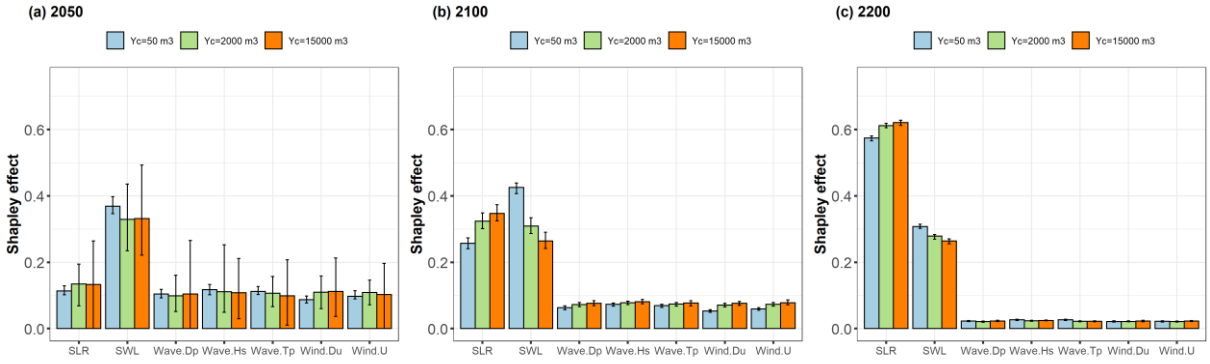

Figure S9: Shapley effects for different volume threshold values Y_C at three time horizons: in the short term, by 2050 (a); in the long term by 2100 (b) and in the very long term by 2200 (c). The green bars correspond to the base case analysed in Sect. 4. The bar height is estimated by the median value over B=50 replicates of the Monte-Carlo-based estimation approach (Sect. 3.5) accounting for GP and sampling error. The lower and upper bounds of the error bar are estimated by using the B=50 replicates.

2. Influence of the RCP scenario

The uncertainty partitioning in Sect. 4 was conducted given the RCP4.5 scenario i.e. given a scenario related to relatively moderate *SLR* magnitude (Fig. 4b), compared to RCP8.5 in particular (Fig. 4c). The analysis is here re-conducted for the two other RCP scenarios. Compared to the base case, Fig. S8(b) indicates that the occurrence of the flooding events for RCP8.5 (respectively RCP2.6) have a higher (lower) probability by about ~20% (-7%) for time horizon 2100. Regarding the time evolution of the Shapley effects, it appears to be the same regardless of the scenario in the short term (Fig. S10a), but starts to differ in the long term (Fig. S10b) and even more significantly in the very long term (Fig. S10c). We note that for RCP8.5, the influence of *SLR* is lower by almost 8% relative to RCP2.6, which is translated into a higher influence of *SWL*.

Like for the threshold value, this is the "offset" effect of *SLR* that influences the most: for RCP8.5, the mode of the *SLR* distribution (in red in Fig. 4c) exceeds the one of the other scenarios after 2100, and can induce a high water level at the coast, hence potentially a water volume value close to Y_C=2,000 m^3, and a higher flooding likelihood. This means that *SLR* values sampled around the mode will less impact the occurrence of the flooding event (and the flooding probability), because a small *SLR* offset is here necessary to trigger the flooding event. This is not the case for the two remaining scenarios, because the mode is of lower magnitude and any *SLR* values sampled above it will have a key impact on the flooding occurrence.

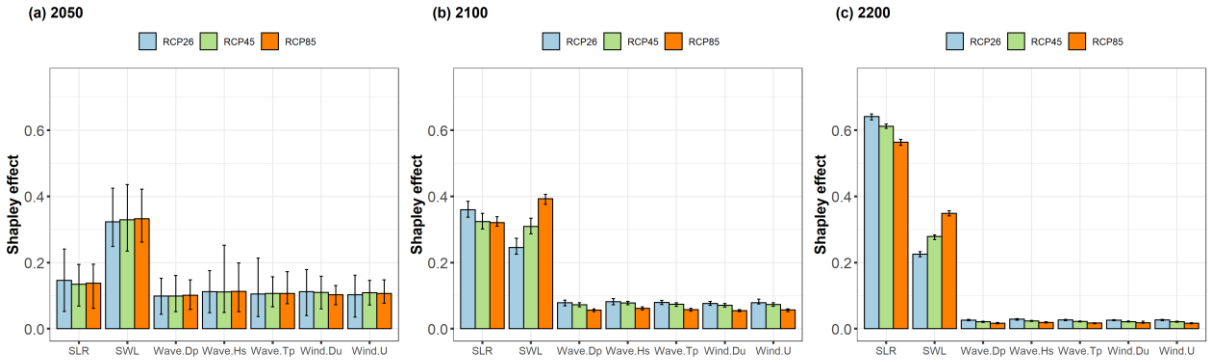

Figure S10: Shapley effects for different RCP scenarios at three time horizons: in the short term 2050 (a); in the long term by 2100 (b) and in the very long term by 2200 (c). The green bars correspond to the base case analysed in Sect. 4. The bar height is estimated with the median value calculated with B=50 replicates of the estimation approach (Sect. 3.5) accounting for GP and sampling error. The lower and upper bounds of the error bar are estimated using the B=50 replicates.

3. Influence of DEM

The flooding simulations described in Sect. 2 were performed using a DEM that is representative of the conditions of 2015. Here, we investigate to which extent an alternative DEM might change the sensitivity analysis results. To do so, we use the DEM 2008 (with the same resolution of 3m than DEM 2015), which corresponds to the conditions before the major flooding event of Johanna 2008 i.e. prior to the protectives measures relying on the raise of the dykes in the aftermath of this event. This means that DEM 2008 presents some sectors of lower topographic elevation of coastal defences compared to DEM 2015 (in particular on the south-eastern sector, which is highly exposed to storm impacts; see Supplementary Materials S4).

Fig. S8(c) shows the time evolution of P_f for both DEMs: this indicates that the changes in topography leads to higher values relative to DEM 2015 before 2100 (with a ratio $P_f^{\mathrm{DEM2008}} / P_f^{\mathrm{DEM2015}}$ of ~14 for 2050). A reverse tendency after 2100 (with a ratio $P_f^{\mathrm{DEM2008}} / P_f^{\mathrm{DEM2015}}$~0.75 for 2200) is however noticed in the very long term. These differences in the short/long term were expected due to the lower elevation in some sectors of DEM 2008, but they remain more difficult to explain in the very long term. An extraction of the forcing conditions (Fig. S11) that lead to exceeding Y_C=2,000 m^3 by 2200 for DEM 2015 but not for DEM 2008, reveals that the differences in P_f are related to particular storm events with moderate-to-high *SLR* level, small-to-moderate wave and wind contributions and higher wave direction (with higher mode at ~265°). This explorative analysis points out the importance of the forcing conditions in the occurrence of the flooding, which is further analysed with the Shapley effects in Fig. S12.

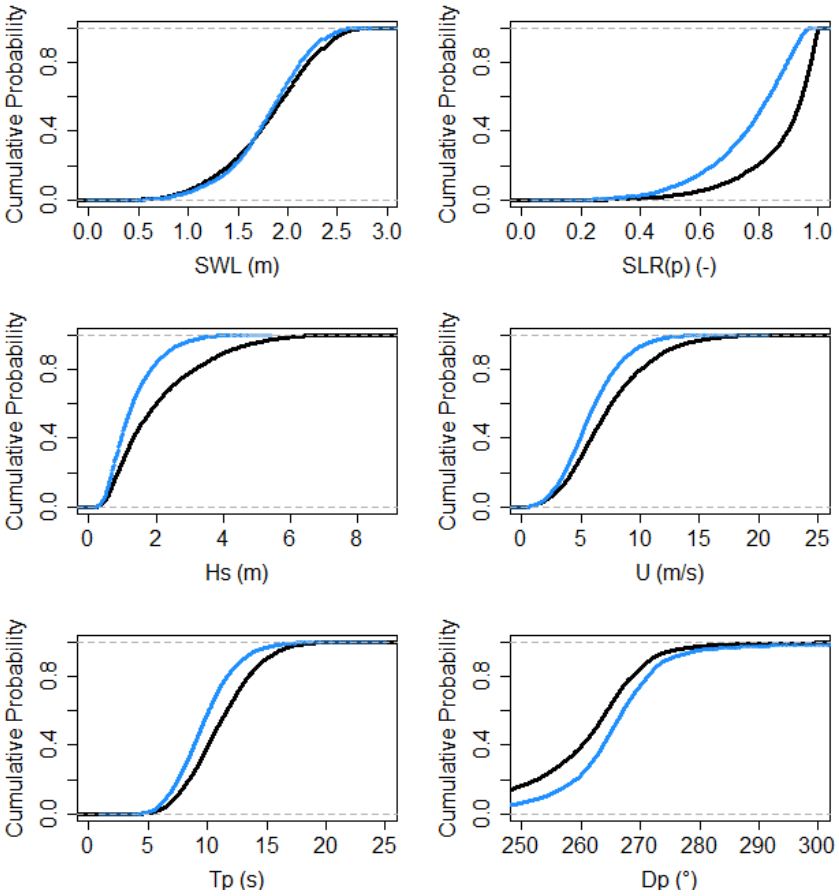

Figure S11: Empirical cumulative probability distribution calculated for N=50,000 random forcing conditions that lead to exceeding Y_C=2,000m3 by 2200 for both DEMs (DEM 2008 and 2015, black) and for DEM 2015 but not for DEM 2008 (light blue). *SLR*(p) denotes the percentile level of the *SLR* time series. The wind direction is not plotted because of the very minor changes between both distributions.

Before 2100, Fig. S12a,b shows that the influence of wave characteristics, *Hs*, *T*p, and *D*p, is higher for DEM 2008 of the order of ~10-18% while the influence of wind characteristics (*U* and *Du*) remains moderate (<10%). There are also differences in the influence of *SLR* with a lower contribution for DEM 2008 (compensated by a higher influence of *SWL*). These differences increase over time until reaching values >30% (Fig. S12c). These results relate to the different drivers of flooding depending on the DEM: the sectors with lower topographic elevation are known have a higher sensitivity to wave-induced flooding, i.e. overtopping at least until 2100. In the very long term, both cases present a small-to-moderate influence of wave characteristics (<10%), hence indicating a lower contribution of overtopping.

Our analysis illustrates how adaptation measures mainly based on raising dykes might affect the drivers of the different flooding processes (overtopping, overflow or combined), but also its complexity. Though all physical processes are not fully understood here (in particular in the very long term, >2100), our results justify deepening the analysis through complementary investigations for instance based on numerical simulations.

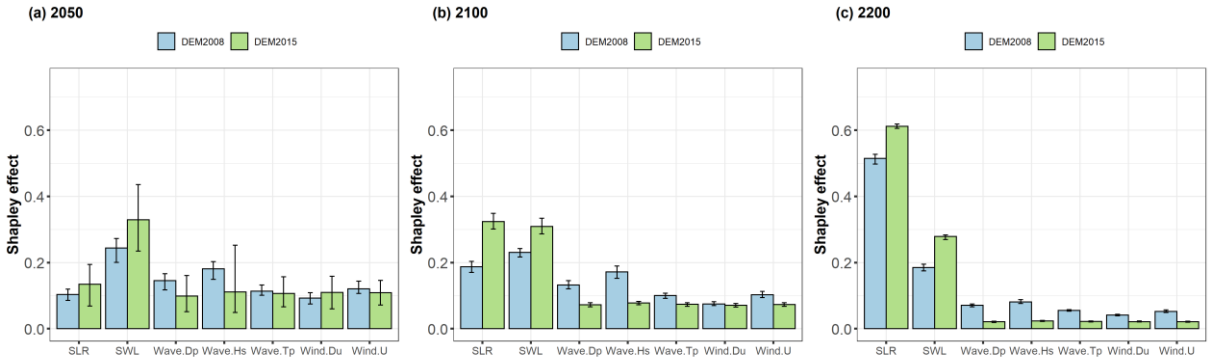

Figure S12: Shapley effects for two different DEMs at three time horizons: in the short term 2050 (a); in the long term by 2100 (b) and in the very long term by 2200 (c). The green bars correspond to the base case analysed in Sect. 4. The bar height is estimated with the median value calculated with B=50 replicates of the estimation approach (Sect. 3.5) accounting for GP and sampling error. The lower and upper bounds of the error bar are estimated using the B=50 replicates.

4. Influence of wave stochasticity

The effect of wave stochasticity was tested by re-conducting the whole analysis but using the 1st quartile (denoted Q_{25}), or the 3rd quartile (denoted Q_{75}) instead of the median (denoted Q_{50}) of *Y*. Figure S8(d) confirms the very minor influence of wave stochasticity on the flooding probability estimate (with differences <1%). The uncertainty partitioning is also very little influenced (Fig. S13) whatever the time horizon. This result differs from the one of Idier et al. (2020b), who showed the importance of this effect that was there comparable to the one of *SLR* as long as the still water level remains smaller than the critical level above which overflow occurs. The differences between both studies may be explained by the differences in the procedure. Idier et al. (2020b) analysed this effect for two specific past storm events, whereas our study covers a large number of events by randomly sampling different offshore forcing conditions (Fig. 3). To conclude on this effect (relative to the others), further investigations are thus necessary and could benefit for instance from recent GSA for stochastic simulators (Zhu and Sudret, 2021).

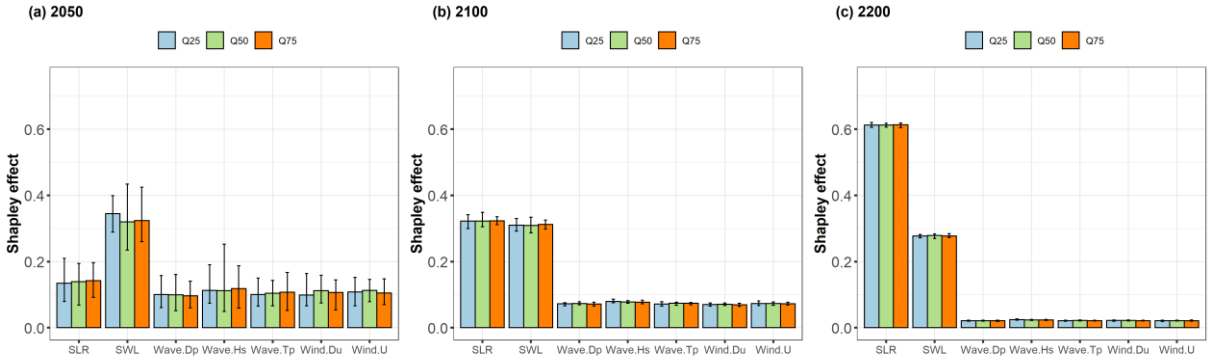

Figure S13: Shapley effects using quartiles (denoted Q_{25},Q_{50},Q_{75}) of the water volume at three time horizons: in the short term 2050 (a); in the long term by 2100 (b) and in the very long term by 2200 (c). The green bars correspond to the base case analysed in Sect. 4. The bar height is estimated with the median value calculated with 50 replicates of the estimation approach (Sect. 3.5) accounting for GP and sampling error. The lower and upper bounds of the error bar are estimated using the B=50 replicates.